RESEARCH PAPER

Numerical analysis of high frequency pulsating flows through a diffuser-nozzle element in valveless acoustic micropumps

Majid Nabavi · Luc Mongeau

Abstract The concept of a valveless acoustic micropump was investigated. Two-dimensional, time-varying, axisymmetric, incompressible viscous flows through a planar diffuser-nozzle element were analyzed for applications in valveless acoustic micropumps. The diffuser divergence half-angles (θ), and the maximum pressure amplitudes (P) were independently varied. The inflow was periodic and the excitation frequency (f) was varied over the range $10\text{ kHz} \leq f \leq 30\text{ kHz}$. The net time-averaged volume flux and the rectification capability of the diffuser were found as functions of θ, f, and P. The phase difference between pressure and velocity waveforms, the life time and the size of large scale flow recirculation regions inside the microdiffuser, and energy losses were found to be strongly frequency dependent.

Keywords Acoustic micropumps · Acoustic standing waves · Microdiffuser · Numerical analysis

List of symbols

ΔP	Pressure drop (Pa)
δ	Stokes layer thickness (m)
η	Rectification capability
λ	Acoustic wavelength (m)
μ	Shear viscosity (kg/m s)
v	Kinematic viscosity (m²/s)
ω	Angular frequency (rad/s)
ρ	Density (kg/m³)
θ	Diffuser divergence half-angle (°)
ξ_d	Pressure loss coefficient in the diffuser direction
ξ_n	Pressure loss coefficient in the nozzle direction
D_h	Hydraulic diameter of the microdiffuser at the inlet (m)
f	Excitation frequency (Hz)
I	Flow inductance (kg/m⁴)
I_d	Flow inductance in the diffuser direction (kg/m⁴)
I_n	Flow inductance in the nozzle direction (kg/m⁴)
N	Cell numbers
P	Maximum pressure (Pa)
p	Pressure (Pa)
p_0	Static pressure (Pa)
Q	Volumetric flow rate (m³/s)
Q_{net}	Net flow rate (m³/s)
R	Flow resistance (kg/m⁴ s)
R_d	Flow resistance in the diffuser direction (kg/m⁴ s)
R_n	Flow resistance in the nozzle direction (kg/m⁴ s)
Re	Reynolds number
T	Excitation period (s)
t	Time (s)
U	Maximum velocity (m/s)
u	Velocity in x direction (m/s)
v	Velocity in y direction (m/s)
V_{net}	Sectional net velocities (m/s)
Wo	Womersley number
x	Axial position (m)
x_{max}	Maximum fluid displacement during one oscillation cycle (m)
y	Transverse position (m)
Z	Flow impedance (kg/m⁴ s)
Z_d	Flow impedance in the diffuser direction (kg/m⁴ s)
Z_n	Flow impedance in the nozzle direction (kg/m⁴ s)

M. Nabavi (✉) · L. Mongeau
Department of Mechanical Engineering, McGill University,
Montreal, Canada
e-mail: majid.nabavi@mail.mcgill.ca

1 Introduction

Micropumps have been proposed for possible applications in small scale fluid machinery (Jang and Kan 2007; Hsu et al. 2007; Cui et al. 2007). Micropumps may be designed with different actuation mechanisms. Piezoelectric, shape memory alloys, electrostatic, electromagnetic and thermal actuators have been proposed (Zhang et al. 2007).

Micropumps may be divided into two categories according to the way fluid is displaced. Hydrodynamic micropumps such as elctrohydrodynamic (Ehlert et al. 2008), magnetohydrodynamic (Nguyen and Kassegne 2008) and electroosmotic (Wu et al. 2005; Park and Lim 2008) micropumps involve a continuous energy source that produces a steady force on the fluid. Positive displacement micropumps add energy periodically by applying a force to one or more movable pump chamber walls. Volume changes resulting from the diaphragm motion impart a direct pressure to the fluid and force fluid mass through the outlet, producing a pulsating flow. Iverson and Garimella (2008) presented a review of micropumping strategies reported in the literature.

Reciprocating valveless micropumps are the most-common type of positive displacement micropumps. They involve the oscillation of a diaphragm excited by an actuator, propelling the flow through two diffuser-nozzle elements which direct the flow (Stemme and Stemme 1993). Gerlach et al. (1995) presented the working principle of a reciprocating micropump and discussed its basic parameters. Olsson et al. (1999) performed a numerical study of a valveless diffuser pump using lumped-mass models. Their results indicated that a low pressure inside the micropump chamber is a limiting factor for the performance of reciprocating valveless micropumps. Pan et al. (2001) suggested an optimal frequency range for reciprocating valveless micropumps based on an analytical model. Hwang et al. (2008) developed a numerical model using ANSYS to evaluate the flow rate of a reciprocating valveless micropumps. Tsui and Lu (2008) analyzed the flow in a reciprocating valveless micropump using both numerical and lumped-element methods. They modeled the motion of the membrane by imposing a reciprocating velocity boundary condition. They found a good agreement between numerical predictions and experimental data for various back pressure values. Hsu and Sheen (2008) developed a microfluidic flow-converter that transforms an oscillatory flow into a steady-like flow in a reciprocating-type pumping device.

2 Valveless acoustic standing wave micropumps (ASWMP)

Valveless ASWMP achieve pumping action through the use of acoustic standing waves in confined vessels. This
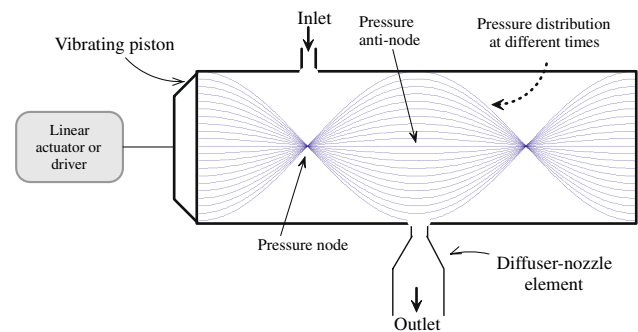

Fig. 1 Schematic of the valveless ASWMP concept

new type of micropump may be categorized as a type of positive displacement micropump. Valveless ASWMP consist of a chamber, a piezoelectric vibrator and a driver (see Fig. 1). The chamber includes fluid inlet and outlet ports. The driver supplies the power to maintain a standing wave in the chamber. The driver impedance must be matched to the acoustic load impedance for optimal electro-acoustic efficiency. The length of the chamber is adjusted so that the traveling wave generated by the acoustic driver is reflected to create constructively interfering standing waves. This arrangement forms a resonant cavity. The standing wave results in one or more pressure nodes and pressure anti-nodes within the chamber. The number of nodes and anti-nodes depends upon the length of the chamber and the excitation frequency. Generally, the pressure at a pressure node is relatively constant at approximately the same level as the ambient pressure in the fluid. The pressure at a pressure anti-node fluctuates above and below the undisturbed pressure level. The inlet and outlet ports are located near the pressure nodes and anti-nodes of the chamber, respectively, as illustrated in Fig. 1. The large pressure fluctuations throughout the resonator, in particular at the pressure anti-node, tend to create a time-averaged net fluid flow through the outlet port. This is because the flow resistance of the diffuser in the outlet port is temporally asymmetric, and is smaller during the portion of the cycle where the pressure at the pressure anti-node exceeds the discharge pressure than during the portion of the cycle where the pressure at the pressure anti-node pressure is smaller than the discharge pressure. As fluid is discharged, there is a reduction in the fluid mass inside the tube which causes a reduction in static pressure. The mean resonator pressure is then lower than the pressure at the inlet. As a result fluid is injected into the resonator through the inlet port. A check valve must be placed at the outlet to prevent the pumped fluid from being re-injected in the resonator during the low pressure portion of the cycle at the pressure anti-node. However, such valves may fail due to wear and fatigue. Thus, only a fixed orifice with a

diffuser-nozzle element is used to achieve pumping action in valveless ASWMP. Among different actuation mechanisms, piezoelectric materials are well suited for valveless ASWMP due to their simple structure, high output power density and high actuation strength. The performance of large scale valved acoustic standing wave pumps has been investigated (Bishop 2000; 2001; Kawahashi et al. 2007). These pumps require one or more check valves at the inlet and the outlet.

In valveless ASWMP, the difference between the forward flow and backward flow resistances of the diffuser is utilized to achieve a net mass flow from the resonator to the outlet reservoir. In previously reported valveless micropumps, a moving diaphragm (deriven by a piezoelectric actuator) does pressure work on the working fluid in a periodic manner. However, in valveless ASWMP, pressure fluctuations are achieved through the establishment of high frequency standing waves inside the micropump chamber. Assuming a linear standing wave inside the chamber, the pressure time history is assumed to be nearly sinusoidal, with a maximum amplitude of P and an angular frequency of ω, $p(t) = P\sin(\omega t)$ at the outlet port (pressure anti-node), and atmospheric at the inlet port (pressure node). When $p(t) > 0$ (the pump mode, Fig. 2a) the diffuser-nozzle element acts as a diffuser and for $p(t) < 0$ (the suction mode, Fig. 2b) the diffuser-nozzle element operates like a nozzle. For equal pressure fluctuation amplitudes in the pump and suction modes, the volume of the outgoing flow through the outlet port is larger than the incoming flow, due to the lower flow resistance in the diffuser direction than that in the nozzle direction. Therefore, a net mass flow rate is achieved. The pumping capacity of the ASWMP is proportional to the pressure fluctuation amplitude inside the pump chamber. To achieve high pressure fluctuations, operation at resonance with sufficiently high force and vibrational displacement are needed.
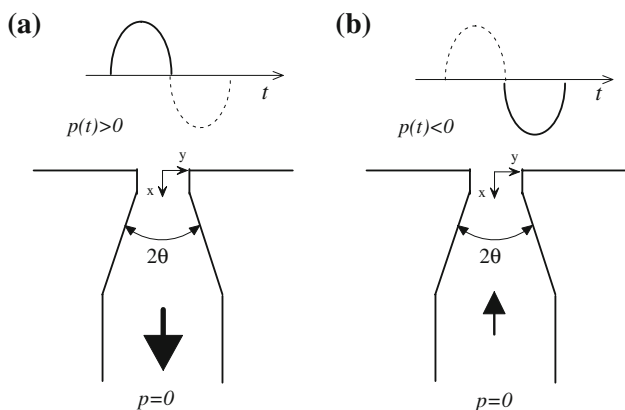

Fig. 2 Flow rectification process in valveless ASWMP, (**a**) pump mode and (**b**) suction mode

One advantage of valveless ASWMP over reciprocating valveless micropumps is that large pressure fluctuation amplitudes may be achieved for comparatively small actuator displacements within the resonator in the valveless ASWMP. Whereas, a low chamber pressure amplitude limits the performance of reciprocating valveless micropumps (Olsson et al. 1999).

3 Energy losses and lumped element model of unsteady flow through the diffuser-nozzle element

The rectification capability (η) of the diffuser-nozzle element can be defined as,

$$\eta = \frac{\xi_n}{\xi_d}, \tag{1}$$

where ξ_n and ξ_d are measures of the direction-dependent flow resistance, called the pressure loss coefficients of the nozzle and diffuser, respectively. These parameters are defined as Stemme and Stemme (1993),

$$\xi_n = \frac{2\Delta P_n}{\rho u_n^2}, \quad \xi_d = \frac{2\Delta P_d}{\rho u_d^2} \tag{2}$$

where ΔP_n and ΔP_d are time-averaged pressure drops in the suction and pump modes, respectively; u_n and u_d are the time-averaged flow velocities in the narrowest part of the diffuser-nozzle element in the suction and pump modes, respectively.

In order to study the unsteady flow, not only flow resistance, but also flow inductance should be considered. One commonly used model for harmonic incompressible viscous flow in a rigid channel consists of the series combination of a resistor (R) and an inductor (I) (Morris and Forster 2004),

$$Z = \frac{\Delta P}{Q} = R + i\omega I, \tag{3}$$

The equivalent electrical analog model of the unsteady flow through the diffuser-nozzle element is shown in Fig. 3. The values of R_d, I_d, Z_d, R_n, I_n, and Z_n are calculated using the equations: $Z_i = \frac{\Delta P_i}{Q_i}$, $\sqrt{R_i^2 + \omega^2 I_i^2} = |Z_i|$, and $\frac{\omega I_i}{R_i} = \tan^{-1}\varphi_i$, where index i represents the diffuser or nozzle directions ($i = d, n$). φ_d and φ_n are the phase difference between pressure and velocity signals in the diffuser direction and the nozzle direction, respectively, which can be calculated from the numerical results.

The total pressure head loss for a diffuser may be defined as,

$$p_L = p_1 + \frac{1}{2}\rho u_1^2 - \left(p_2 + \frac{1}{2}\rho u_2^2\right), \tag{4}$$

where p_1 and p_2 are the pressures at the diffuser inlet and exhaust, respectively, and u_1 and u_2 are the average flow
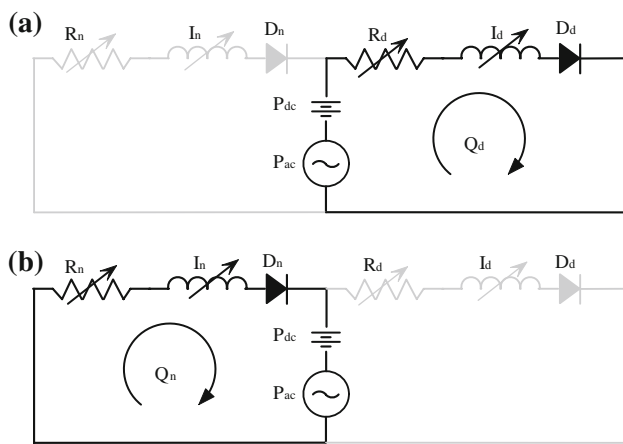
Fig. 3 Equivalent electrical model of the unsteady flow through the diffuser-nozzle element along (**a**) the diffuser direction, and (**b**) the nozzle direction

velocity through the diffuser inlet ($y = 0$) and exhaust ($y = 1{,}800$ μm), respectively. The total energy loss over one period of the excitation signal (T) may then be obtained using,

$$e_L = p_L Q_{\text{net}} T \tag{5}$$

4 Review of previous work

The diffuser-nozzle element plays an important role in the performance of reciprocating micropumps, and in particular valveless ASWMP. Steady flows through diffuser-nozzle elements have been extensively investigated both numerically and experimentally. Singhal et al. (2004) analyzed the steady flow through diffuser-nozzle elements using the commercially available software Fluent. They observed that flow rectification through the diffuser-nozzle element is possible for very low Reynolds number laminar flows. Experimental investigations of the performance of diffuser-nozzle elements were performed by Yang et al. (2004). They found that the pressure loss coefficients of the nozzle and diffuser decreased as the Reynolds number was decreased, resulting in an increased rectification capability. Sun and Yang (2007) investigated the effects of the diffuser half angle on the flow rectification of a microdiffuser in the steady flow regime. Their results showed that the flow rate in the diffuser direction was always larger than that in the nozzle direction for $5° \leq \theta \leq 55°$ regardless of the half angle. Wang et al. (2009) investigated the loss characteristics and flow rectification performance of flat-walled microdiffuser valves for Reynolds numbers between 100 and 2000. They reported

that flow separation plays a significant role in reducing diffuser loss. The diffuser angle for optimum diffuser efficiency was found to decrease from 40° at $Re = 100$ to 20° for $Re > 500$.

All the above-mentioned studies of flows in diffuser-nozzle elements were performed in the steady flow regime. Sun and Huang (2006) performed a numerical study of the unsteady flow through a microdiffuser for frequencies up to 1 kHz. They found that microdiffusers with larger half angles feature better rectification capability for $5° \leq \theta \leq 35°$. The net flow rate obtained was nearly independent of θ, for $\theta > 35°$. Experimental investigations of the unsteady flow in a diffuser-nozzle element were performed by Sheen et al. (2008). They measured the transient flow behavior in an obstacle-type valveless PZT micropump using a micro-PIV for excitation frequencies in the range 1 kHz $\leq f \leq$ 3 kHz. They observed and quantified the flow recirculation around the obstacle, and concluded that such flow behavior could enhance the flow rectification capability.

The minimum possible length of a valveless ASWMP is one-quarter wavelength ($\lambda/4$). Therefore, the excitation frequency should be high to limit the chamber length. Frequencies greater than 10 kHz, for example, are required to keep the length of the micropump smaller than around 1 cm for pumping air. This frequency range is far greater than that of reciprocating valveless micropumps. Pulsating flows through microdiffusers have not yet been investigated at such high frequencies. The present study attempts to partly fill this gap. High frequency (10 kHz $\leq f \leq$ 30 kHz) oscillatory flows through diffuser-nozzle elements were numerically modeled for different divergence angles and maximum pressure amplitudes. The phase difference between pressure and velocity waveforms, the life time and size of the flow circulation regions inside the microdiffuser, and energy losses were found to be significantly different at high frequencies from observed behavior at low frequencies.

5 Numerical procedures

The commercially available software Fluent, which is based on a finite-volume scheme was used to discretize the governing equations. The working fluid considered was water, with a density of $\rho = 998.2$ kg/m^3 and a viscosity of $\mu = 0.001003$ kg/m s. The flow was assumed to be laminar and incompressible. No-slip boundary conditions were applied at the walls. The imposed pressure at the inlet and the outlet were $P\sin(2\pi ft)$ and zero, respectively. Unsteady flow simulations were carried out for $15° \leq \theta \leq 60°$. A transient axisymmetric solver was used. Figure 4 shows the 2-D computational domain.
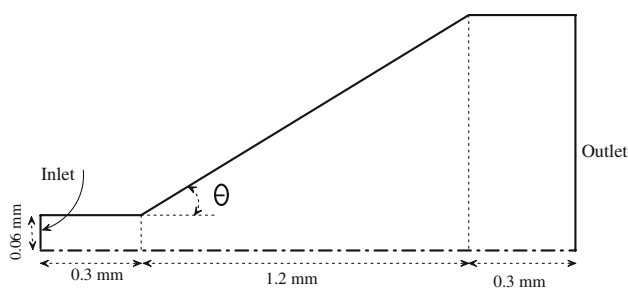
Fig. 4 Schematic of the geometry and dimensions of the microdiffuser

The governing equations are:

$$\frac{\partial u}{\partial x} + \frac{\partial v}{\partial y} = 0, \tag{6}$$

$$\rho\left(\frac{\partial u}{\partial t} + u\frac{\partial u}{\partial x} + v\frac{\partial u}{\partial y}\right) + \frac{\partial p}{\partial x} = \mu\left(\frac{\partial^2 u}{\partial x^2} + \frac{\partial^2 u}{\partial y^2}\right), \tag{7}$$

$$\rho\left(\frac{\partial v}{\partial t} + u\frac{\partial v}{\partial x} + v\frac{\partial v}{\partial y}\right) + \frac{\partial p}{\partial y} = \mu\left(\frac{\partial^2 v}{\partial x^2} + \frac{\partial^2 v}{\partial y^2}\right), \tag{8}$$

and initial conditions are $u(x, y, 0) = 0$, and $v(x, y, 0) = 0$.

In order to minimize numerical diffusion, a second order up-wind differencing scheme was used for the solution of the momentum equation. A pressure-implicit with splitting of operators (PISO) was used as the pressure–velocity-coupling scheme, which is recommended for transient calculations. The use of PISO allowed for a rapid rate of convergence without any significant loss of accuracy (Issa 1986; Ferzieger and Peric 1996). Pressure was discretized with a pressure-based segregated solver only (PRESTO) scheme. Other schemes (linear or second-order schemes) lead to strong divergence or to slow convergence (Patankar 1980). The under relaxation factors used for pressure and momentum were set equal to 0.6 and 0.4, respectively. A second order up-wind scheme was used to evolve the solution over time. A time step value of one hundredth of the oscillation period was used throughout the simulations.

5.1 Computational grid

A structured grid was used for the inlet and outlet regions, while an unstructured grid was used for the diffuser region. It was found that the velocity fields had a lower sensitivity to grid size for the mixed grid (Sun and Huang 2006). The cell numbers (N) were varied from 4,000 (for $\theta = 15°$) to 8,000 (for $\theta = 60°$), and the average mesh size was approximately 100 μm^2 and 170 μm^2, for $\theta = 15°$ and for $\theta = 60°$, respectively. The grid structure featured very fine grids in the vicinity of the microdiffuser wall, and the grid density decreased near the centerline. The mesh size was smaller in the inlet region than that in the outlet region.
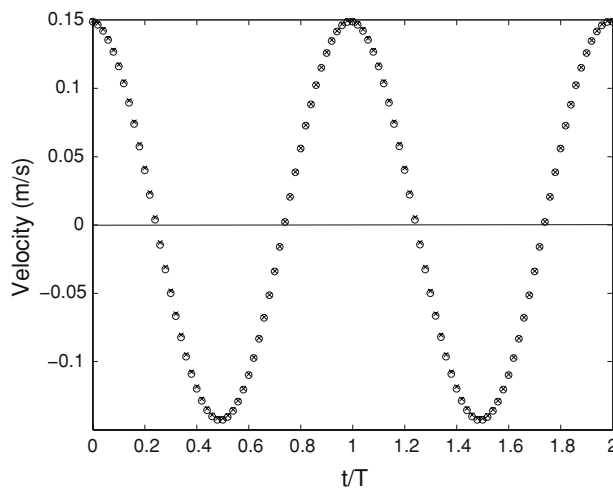

Fig. 5 The velocity time history over two periods of oscillation for $f = 10$ kHz, $P = 5,000$, and $\theta = 15°$, for $N = 4,000$ (×) and $N = 10,000$ (○)

A grid refinement test was undertaken to examine the sensitivity of the solution to grid spacing. For an excitation frequency of $f = 10$ kHz, a peak pressure value of $P = 5,000$ Pa, and a half angle of $\theta = 15°$, N was increased from 4,000 to 10,000. The velocity time history for the two cases over two periods of oscillation are shown in Fig. 5. This figure clearly shows that the use of denser computational grids did not change the results significantly. The relative differences in net velocity for these two cases was found to be 0.52%. A single mesh was used over the entire range of oscillation frequencies.

Increasing the number of time steps per cycle from 100 to 200 resulted in no significant change in the velocity field. A total of 200–300 cycles were required to eliminate the effects of the initial transient and reach a stable periodic velocity variation. Only a few cycles were required for this purpose at low frequency ($f < 500$ Hz).

5.2 Model verification

To verify the accuracy of the numerical model to simulate the oscillatory flow in microchannels, results for pulsating, laminar oscillatory flow in a 2-D microchannel of width $2a$ and length L driven by a sinusoidal pressure gradient $\partial p/\partial x = p^* e^{i\omega t}$ were compared with the analytical solution. Following Cosgrove et al. (2003), the analytical expression for the y-dependent axial velocity in the microchannel is

$$u = \Re\left\{\frac{p^*}{i\omega\rho}\left[1 - \frac{\cosh[y(\alpha + i\alpha)/\sqrt{2}a]}{\cosh[(\alpha + i\alpha)/\sqrt{2}]}\right]e^{i\omega t}\right\}, \tag{9}$$

where $\alpha = a\sqrt{\omega/v}$, and $\Re$ denotes the real part of the solution. For large α, Eq. 9 reduces to
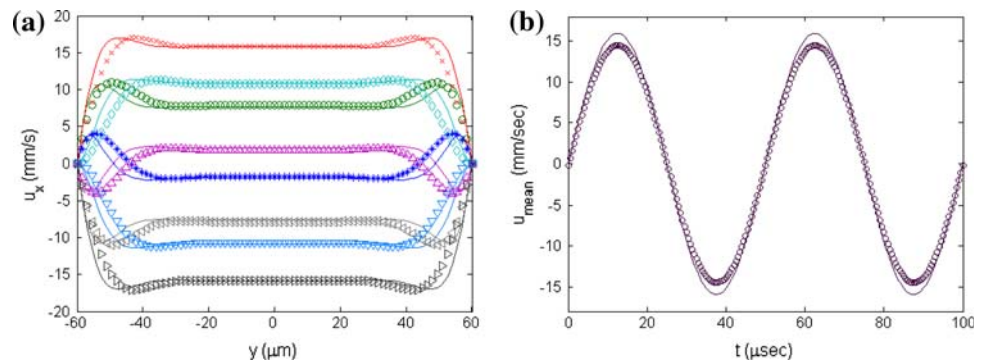
$$u \simeq u_m \sin \omega t, \tag{10}$$

where $u_m = \frac{p^*}{\omega\rho}$. The time-oscillating axial velocity is then uniform across the microchannel. The mean velocity is obtained as,

$$\bar{u} = \frac{1}{T}\int_0^T u(y,t)\mathrm{d}t \simeq \frac{2p^*}{\pi\omega\rho}. \tag{11}$$

Fig. 6a shows velocity profiles from numerical predictions and the exact solutions from Eq. 9 for $f = 10$ kHz, $a = 60$ μm, $L = 1,000$ μm, and $P = 1,000$ Pa, ($p^* = 2,777,777$ Pa/m). The value of α for this case was 15. Fig. 6a shows the velocity profiles at phases $\omega t = 0$, $\pi/5$, $\pi/2$, $4\pi/5$, π, $6\pi/5$, $3\pi/2$, $9\pi/5$. The overall difference between the analytical (u_a) and numerical (u_n) velocity across the microchannel at 100 discrete phases over one period ($\varepsilon = \Sigma_t\Sigma_y|u_n(y,t)-u_a(y,t)| \, / \, \Sigma_t\Sigma_y|u_a(y,t)|$) was found to be 6.9%. The velocity time history of the analytical and numerical models over two periods of oscillation are shown in Fig. 6b. The good agreement in shape and amplitude between the analytical and numerical results support the accuracy of the numerical model.

Further verifications were made through comparisons with 3-D numerical simulations performed by Sun and Huang (2006). For the same geometry, in 2-D, the time-dependent pressure and flow rate for $\theta = 25°$, $f = 100$ Hz and $P = 200$ Pa are plotted in Fig. 7. The flow rate time history was calculated and became periodic after the first cycle. The amplitude of the flow rate signal and its phase in relation to that of the pressure are in good agreement with the 3-D simulation results of Sun et al. (see Fig. 1b of Sun and Huang (2006)).

5.3 Symmetry considerations

The validity of choosing an axisymmetric domain was also verified. Although the diffuser is symmetric, previous numerical and experimental investigations showed that steady, incompressible, laminar flow in a symmetric diffuser may be asymmetric at high values of Reynolds
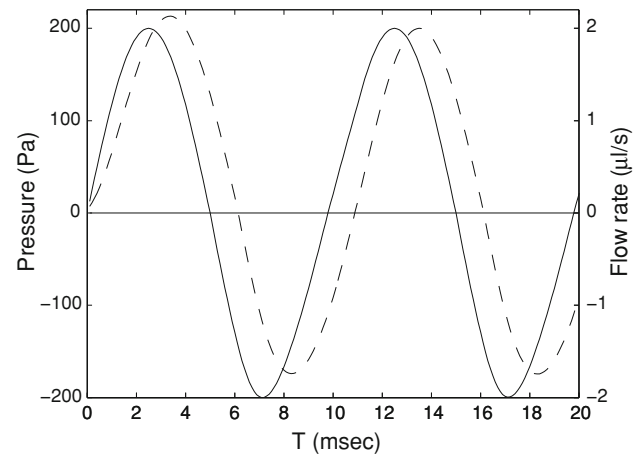

Fig. 7 The time-dependent pressure (*solid line*) and flow rate (*dashed line*) for $\theta = 25°$, $f = 100$ Hz and $P = 200$ Pa

number. There is a critical *Re* beyond which the flow is asymmetric (Durst et al. 1974; Tsui and Wang 1995). The origin of the asymmetry is related to the instability of the shear layers formed by flow separation. The instability originates from small periodic perturbations in the shear layers, amplified to form wavy flow patterns, and eventually vortex-like structures as they are convected downstream (Tsui and Wang 1995).

In order to verify the symmetry of the unsteady flow pattern in the microdiffuser, an extended 2-D domain with $\theta = 30°$ was considered. For an inlet pressure of 120 Pa in the steady laminar flow regime, the flow is asymmetric as shown in Fig. 8a. However, in the unsteady laminar flow regime, symmetric flows were observed for different amplitudes and frequencies of the inlet pressure. A sufficiently long discharge duct section prevented the uniform outlet boundary conditions to enforce a symmetric pattern outflow. Figure 8b, c shows the velocity amplitude in the microdiffuser for $f = 10,000$ Hz, and $P = 30,000$ Pa for two different phases of the pressure signal ($\pi/2$ and π). The maximum Reynolds number for both the steady and the unsteady cases was around 51. The above analysis showed that the oscillation period was too short to allow the

Fig. 8 The stream function contours for (**a**) steady flow regime ($P = 120$ Pa, $Re = 51$), and unsteady flow regime ($P = 30{,}000$ Pa, $f = 10{,}000$ Hz, $Re_{max} = 51$, at two different phases of the pressure signal (**b**) $\pi/2$, and (**c**) $\pi/2$
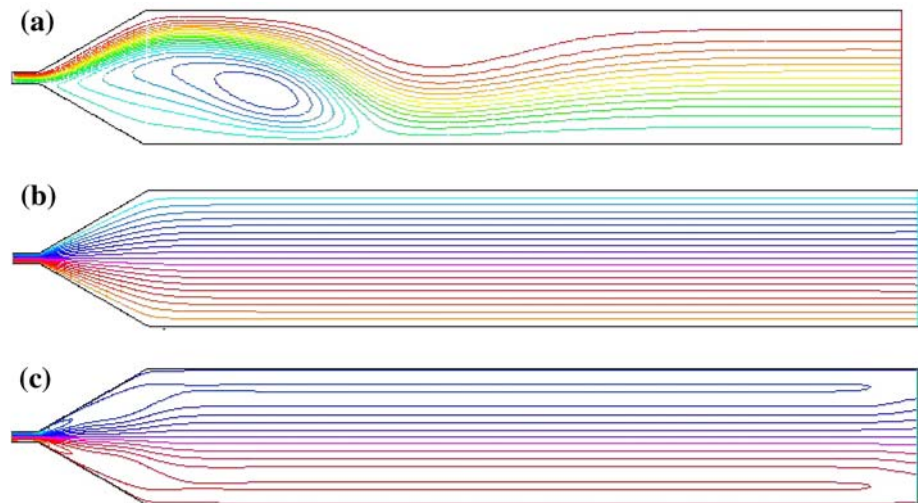
instability of the shear layers to develop, and asymmetric flow separation to occur.

6 Results and discussion

A total of 24 cases were considered for excitation frequencies of $f = 10$, 20 and 30 kHz, maximum pressure values of $P = 5{,}000$ and 10,000 Pa, and half angle values of $\theta = 15°$, $30°$, $45°$, and $60°$, In addition, three low frequency cases ($f = 100$ Hz, and $\theta = 15°,30°$, and $45°$) were studied for comparison with the high frequency cases.

6.1 Time-varying velocity signals

The time-dependent pressures and average velocities at the microdiffuser inlet are shown in Fig. 9 for $\theta = 15°$, $30°$, and $45°$ at high frequency ($f = 10{,}000$ Hz, left pane) and low frequency ($f = 100$ Hz, right pane). The maximum pressure for the high frequency cases was $P = 10{,}000$ Pa. For low frequency cases, the pressure was selected to produce almost the same maximum velocity as for the corresponding high frequency case. For all cases, the time-varying mean velocities are not temporally symmetric, although the pressure variations are symmetric. The mean velocities in the diffuser direction (positive cycles) are larger than those in the nozzle direction (negative cycles). This is due to a lower flow resistance in the diffuser than in the nozzle direction. The ratio between the maximum velocity in the diffuser and that in the nozzle direction is a function of θ.

The phase difference between pressure and velocity signals at high frequency is almost $\pi/2$, in contrast with the low frequency case, where the phase difference is considerably less than $\pi/2$ (see Fig. 9). This is due to the fact that at high frequencies the flow impedance (Z) is almost purely

inductive (Eq. 3), and the effect of R on Z is almost negligible. At low frequencies, both R and I contribute to Z, due to smaller value of ω.

6.2 Two-dimensional time-dependent velocity profiles

The time-dependent stream function (ψ) contours were obtained for both low and high frequency cases ($f = 100$ and 10,000 Hz) and for $\theta = 15°$ and $45°$. Figure 10 shows stream function contours for $\theta = 15°$, $f = 100$ and 10000 Hz, for six different phases of the inlet pressure waveform, which are also shown in the figure. It is noteworthy that the phase difference between the pressure and velocity waveforms for high and low frequency cases are around $\pi/2$ and $2\pi/11$, respectively. As shown in Fig. 10, flow separation due to adverse pressure gradient is observed at both high and low frequency. At low frequency, flow separation occurs before the inlet pressure signal changes sign (see Fig. 10b1), and persists over almost 20% of the period. At high frequency, flow separation was not observed when the inlet pressure sign changed (see Fig. 10a1). Instead, the onset of flow separation was near the times of maximum and minimum inlet pressure (see Fig. 10a2). This trend was also observed in a microdiffuser of greater half-angle ($\theta = 45°$) as shown in Fig. 11. This figure shows the stream function contours at four different phases of the inlet pressure waveform.

It is important to verify that the flow field in the microdiffuser is not influenced by the outlet boundary. For $f = 100$ Hz, $P = 400$, and $\theta = 15°$, the stream function contours for the original computational domain (Fig. 4) and a computational domain with a longer outlet section (1,000 μm) at the phase of 203° of the pressure signal are shown in Fig. 12. As shown, there in no significant difference in the flow fields.
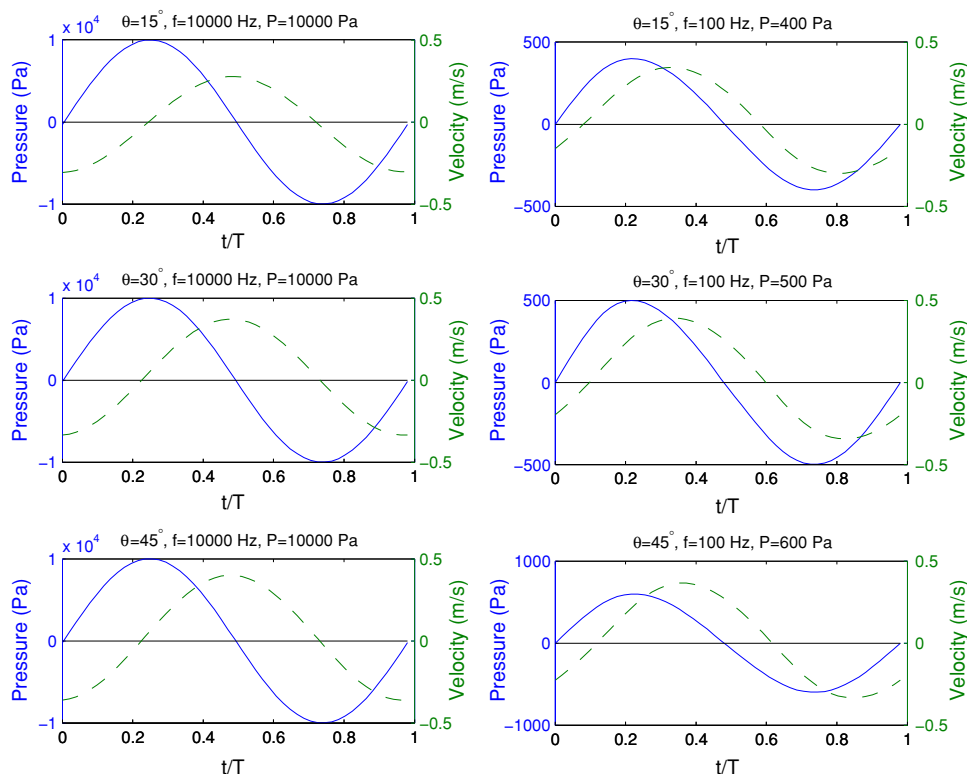
Another important observation is that the life time and size of the flow recirculation region for the low frequency cases is larger than those for the high frequency cases. Consider τ_1 and τ_2 as the fraction of period in which flow separation exists when the inlet pressure decreases and increases, respectively ($0 \le \tau_1, \tau_2 \le 0.5$) and $\tau = \tau_1 + \tau_2$ ($0 \le \tau \le 1$). The values of τ_1, τ_2, and τ for $\theta = 15°$, and 45° for both high and low frequencies are shown in Table 1. The results show that at high frequency, flow separation occurred at 12% and 16% of the period for $\theta = 15°$ and 45°, respectively. These values were 30 and 42% for low frequency cases for $\theta = 15°$ and 45°, respectively.

6.3 Net velocity and rectification capability

The sectional net velocities at the diffuser section of the diffuser-nozzle element and the rectification capability as functions of θ for $P = 5{,}000$ and $10{,}000$ Pa and $f = 10$, 20 and 30 kHz are shown in Fig. 13. A positive net flow rate was achieved using the valveless ASWMP regardless the value of θ. A better pumping action was achieved for greater values of θ. For $\theta > 30°$, a further increase in θ did not result in any significant increase in net velocity. Figure 13 also shows that the rectification capability of the microdiffuser was always greater than unity for the cases studied. These results are in agreement with the low frequency numerical results reported by Sun and Yang (2007).

An increase in excitation frequency resulted in a decrease of net flow rate and rectification capability. An increase in maximum pressure resulted in an increase of net flow rate and rectification capability regardless of frequency, f and half angle, θ.

Using the time-dependent pressures and velocities shown in Fig. 9 and Eq. 3, as well as Fig. 3, the values of flow resistance, inductance, and impedance in the diffuser direction (R_d, I_d, and Z_d, respectively) and the nozzle direction (R_n, I_n, and Z_n, respectively) as a function of θ for $P = 5{,}000$ Pa and $P = 10{,}000$ Pa at two different excitation frequencies $f = 10$ kHz and 20 kHz were calculated and are plotted in Fig. 14. This figure shows that the values of flow resistance, inductance, and impedance in the diffuser direction are lower than those in the nozzle direction. The values of R_d, I_d, Z_d, R_n, I_n, and Z_n decrease as θ increases. An increase in f or a decrease in P cause an increase in R_d and I_d, and a decrease in R_n, I_n, and consequently an decrease in net velocity and rectification capability.

The Womersley number, $Wo = D_h/\delta$, is used to describe the unsteady nature of fluid flow in response to an unsteady pressure gradient. $\delta = \sqrt{v/\omega}$ is the Stokes layer thickness. Small values of Wo (1 or less) indicate that viscous effects are dominant and that the frequency of pulsations is sufficiently low so that a parabolic velocity profile has time to develop during each cycle, and the flow is very nearly in phase with the pressure gradient. In this regime,
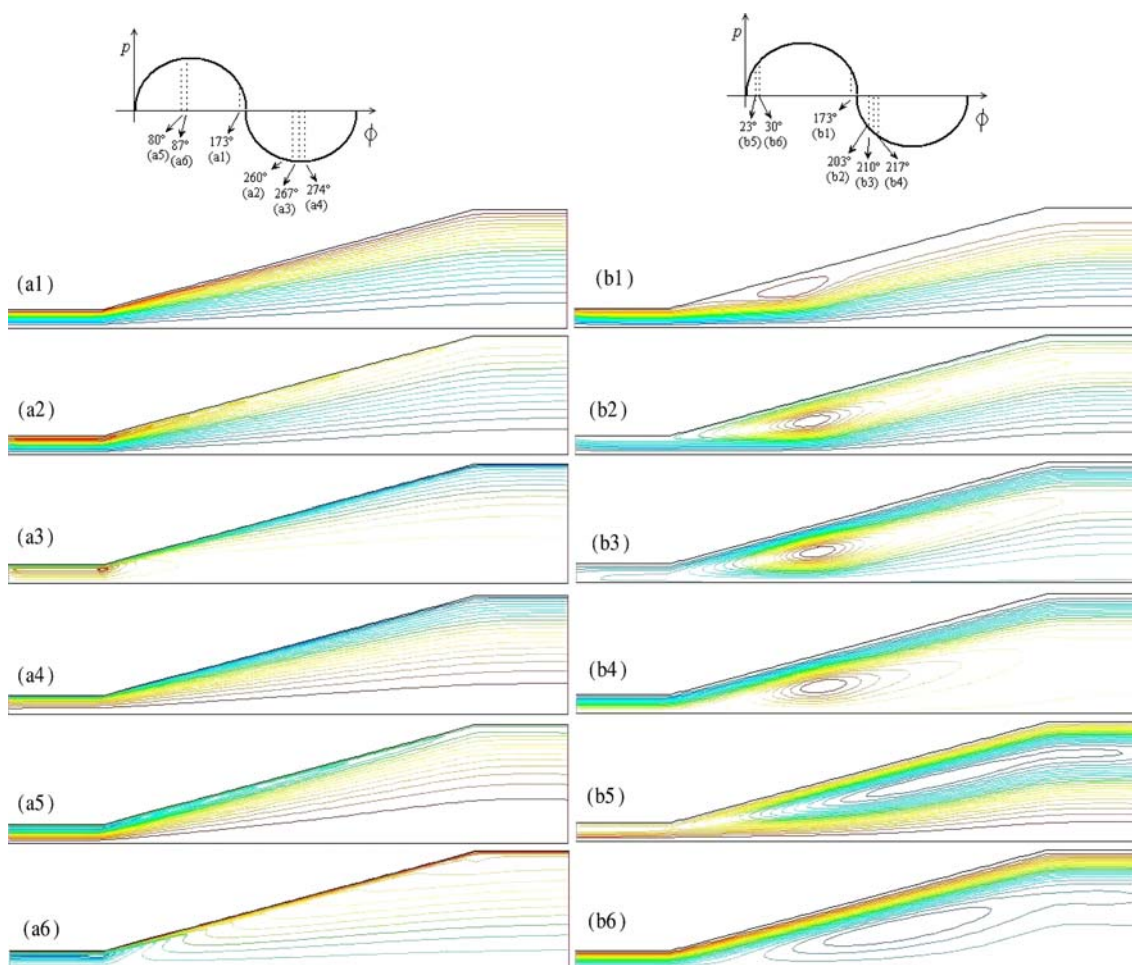
Fig. 10 Time-dependent stream function (ψ) for $\theta = 15°$, $f = 10,000$ Hz (*left pane*) and $f = 100$ Hz (*right pane*)

the microdiffuser performance is frequency-independent. Large values of Wo (20 or more) implies that the frequency of pulsations is sufficiently large that the velocity profile is relatively flat, and the mean flow lags the pressure gradient by about $\pi/2$. For Wo grater than 1, the microdiffuser performance is frequency-dependent. The values of Wo for $f = 10$, 20, and 30 kHz are 46, 68, and 80, respectively. These values are far larger than the value of Wo for $f = 100$ Hz, which is 4.6.

At this point, it is useful to provide support for the validity of the laminar flow assumption for the high frequency pulsating flows considered in this study. Kurzweg et al. (1989) provided a criteria for the transition from laminar to turbulent state in pulsating water flows in pipes based on an experimental investigation. At high Womersley numbers, turbulence first appears when the non-dimensional parameter $\beta = x_{max}/\delta$ exceeds a value of about 700. For the high frequency cases considered in the present study, the maximum value of β was calculated to be about 3.2, which is far smaller than the critical value of β. Furthermore, the maximum Reynolds number, defined

as $Re = UD_h/v$, was about 50. This value is far smaller than the critical Reynolds numbers (200-2300) reported in the literature for transition to turbulence in microchannels. Therefore, the assumption of laminar flow seems warranted for the simulations.

6.4 Energy losses

Figure 15a, b shows p_L versus time (Eq. 4) over one cycle of velocity waveform for $\theta = 30°$ at high frequency ($f = 10,000$ Hz, $P_0 = 10,000$ Pa, left pane) and low frequency ($f = 100$ Hz, $P_0 = 500$ Pa, right pane). It is important to note that the difference between the main diagonal angle of p_L curves is related to the phase difference between pressure and velocity waveforms at high and low frequency (see Fig. 9). The total energy loss, $|e_L|$, (Eq. 5) over one cycle of velocity waveform is shown in Fig. 15c, d. The plots exhibit a hysteretic behavior for both high and low frequencies. The area under the curve represents the total energy loss over one cycle of the excitation signal. Figure 15c, d clearly shows that, the total energy

Fig. 11 Time-dependent
stream function (ψ) for $\theta = 45°$,
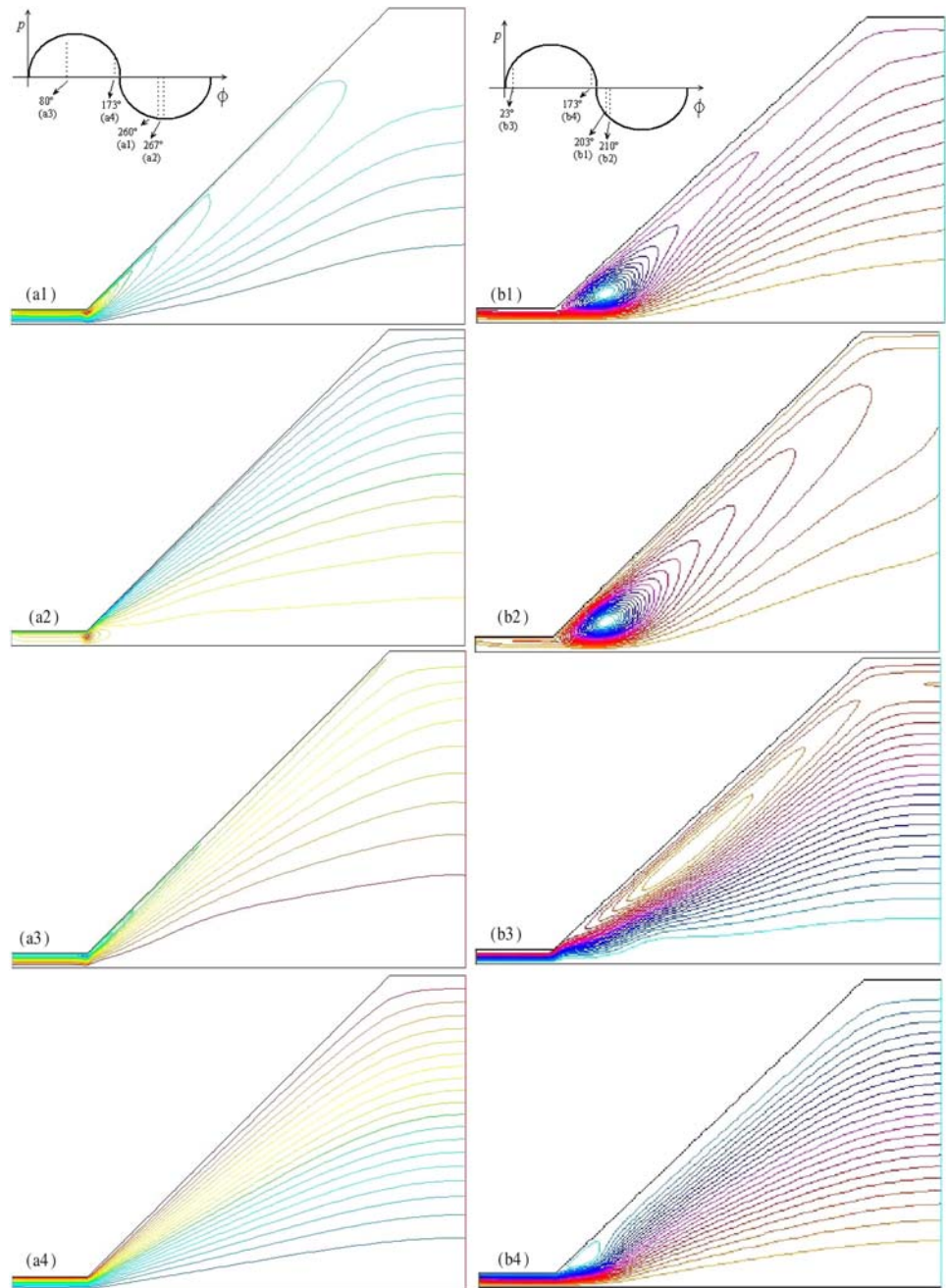$f = 10{,}000$ Hz (*left pane*) and
$f = 100$ Hz (*right pane*)

Fig. 12 The stream function for
the original computational
domain (*bottom*) and a
computational domain with
longer outlet section (*top*) at the
phase of 203° of the pressure
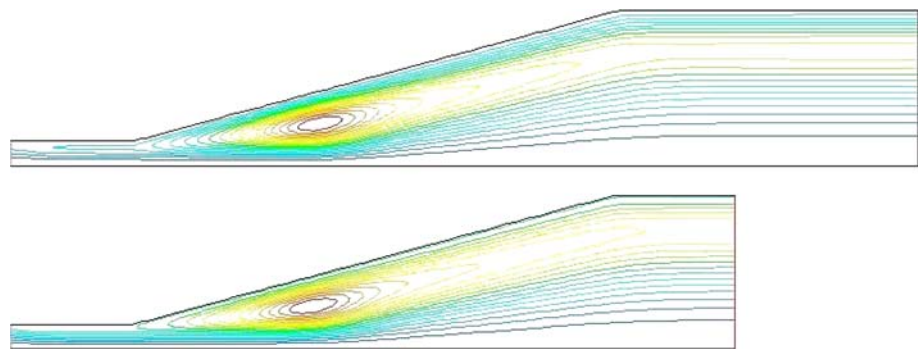signal for $f = 100$ Hz, $P = 400$,
and $\theta = 15°$

Table 1 The values of τ_1, τ_2, and τ for $\theta = 15°$, and $45°$ for both high and low frequency cases

	$f = 10{,}000$ Hz		$f = 100$ Hz	
	$\theta = 15°$	$\theta = 45°$	$\theta = 15°$	$\theta = 45°$
τ_1	0.06	0.08	0.2	0.32
τ_2	0.06	0.08	0.1	0.1
τ	0.12	0.16	0.3	0.42

τ_1 and τ_2 are the fraction of the period in which flow separation exists when the inlet pressure decreases and increases, respectively, $\tau = \tau_1 + \tau_2$

loss over one cycle at low frequency is higher than that at high frequency, although the net flow rates for both high and low frequencies are almost equal. The reason for this phenomenon is that the size and the life time of flow circulation at low frequency is greater than that at high frequency as shown in Figs. 10 and 11 and Table 1.

7 Conclusions

The concept of a valveless ASWMP was investigated. Time-dependent flow structures through the diffuser-nozzle element of this new type of micropump were numerically investigated for different values of the excitation frequency, the divergence angle, and the maximum pressure amplitude. The accuracy of the numerical model for simulations of the oscillatory flow in the microdiffuser was validated using the analytical formula and previous numerical models. The phase difference between pressure and velocity waveforms at high frequency was almost $\pi/2$, whereas this value at low frequencies was significantly less than $\pi/2$. Flow separation was observed for both high and low frequency cases. However, for low frequency cases, flow separation occurred before the inlet pressure signal changed sign, whereas for high frequency cases, the onset of flow separation coincided with the maximum and minimum of the inlet pressure signal. The life time and size of the flow circulation for the high frequency cases were smaller than those for the low frequency cases. Although there is a possibility for asymmetric flow to be established in microdiffuser in the steady laminar flow regime, the unsteady flow was always symmetric and in the laminar flow regime over the values of Reynolds number and divergence angle considered. As for low frequencies, better pumping action was found for microdiffuser with larger divergence angles at high excitation frequencies. Increase of maximum pressure or decrease of excitation frequency resulted in increase of net flow rate and rectification capability. The values of flow resistance, inductance, and impedance in the diffuser direction were lower than those in the nozzle direction. The values of R_d, I_d, Z_d, R_n, I_n, and Z_n decreased as θ increased. An increase in f or a decrease in P caused an increase in R_d and I_d, and a decrease in R_n,

Fig. 13 The sectional net velocities (V_{net}) and rectification capability (η) as a function of θ for $P = 5{,}000$ Pa (°) and $P = 10{,}000$ Pa ($\triangle$) at different excitation frequencies $f = 10$ kHz (*first row*), $f = 20$ kHz (*second row*), and $f = 30$ kHz (*third row*)
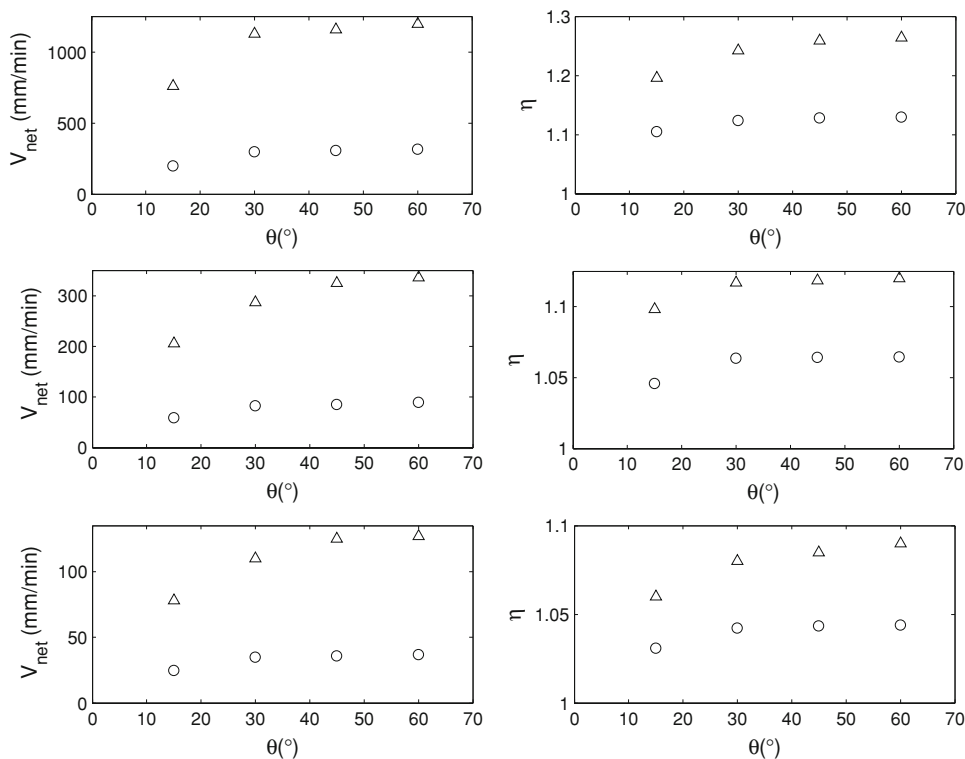
Fig. 14 The variation of R, I, and Z in the diffuser direction ($\triangleright$) and the nozzle direction ($\triangleleft$) as functions of θ for $P = 5{,}000$ Pa (*dotted line*) and $P = 10{,}000$ Pa (*dashed line*) at two different excitation frequencies $f = 10$ kHz (*left pane*), and $f = 20$ kHz (*right pane*)
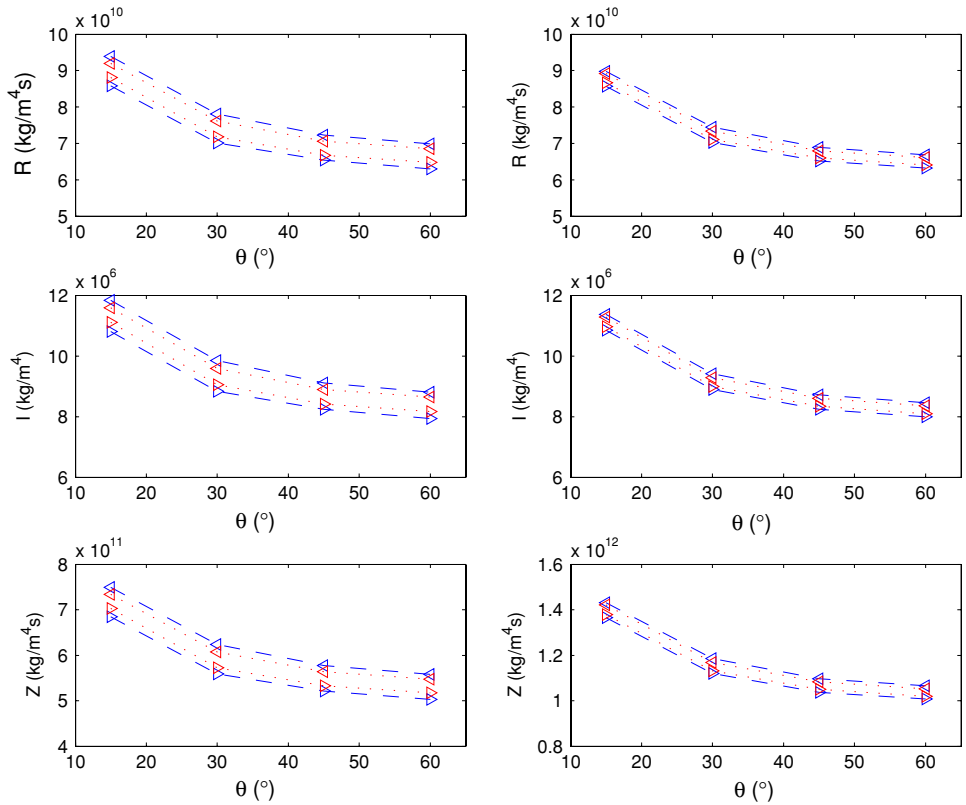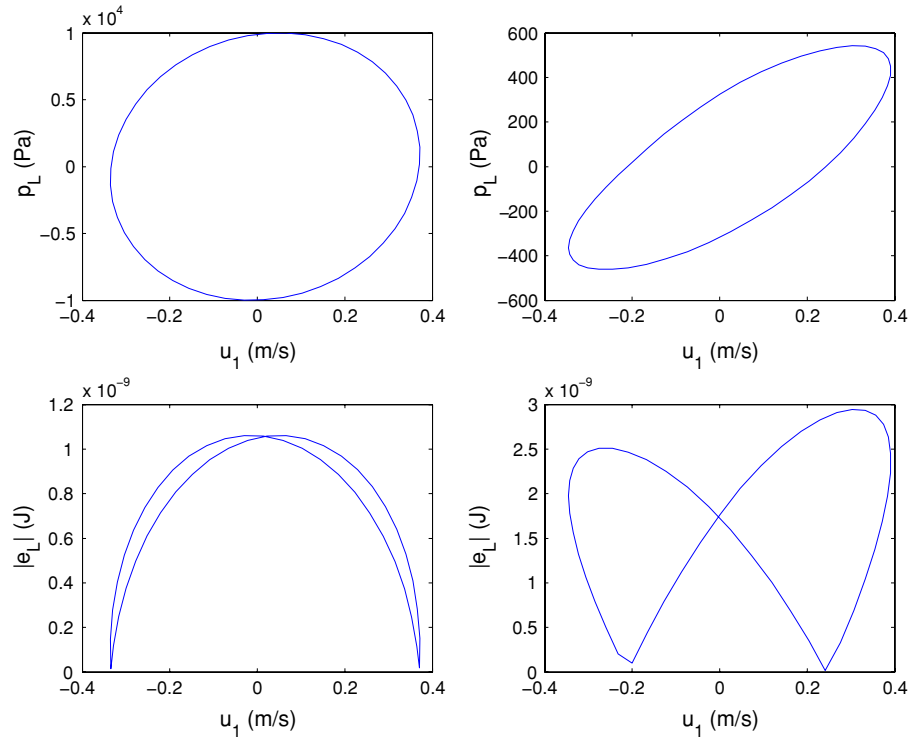

Fig. 15 p_L (*top row*) and $|e_L|$ (*bottom row*) versus velocity over one oscillation cycle for $\theta = 30°$ at high frequency ($f = 10{,}000$ Hz, $P_0 = 10{,}000$ Pa, *left pane*) and low frequency ($f = 100$ Hz, $P_0 = 500$ Pa, *right pane*)

I_n, and consequently an decrease in net velocity and rectification capability. For the same amount of net flow rate, the total amount of energy losses over one cycle at low frequency was greater than that at high frequency. This is due to the smaller size and life time of flow circulation region at low frequency compared to high frequency.

References

Bishop RP (2000) Standing wave pump, US Pat. No. 6079214

Bishop RP (2001) Standing wave pump. J Acoustic Soc Am 109:447–448

Cosgrove JA, Buick JM, Tonge SJ, Munro CG, Greated CA, Champbell DM (2003) Application of the lattice Boltzmann method to transition in oscillatory channel flow. J Phys A: Math Gen 36:2609–2620

Cui Q, Liu C, Zha X (2007) Study on a piezoelectric micropump for controlled drug delivery system. Microfluid Nanofluid 3:377–390

Durst F, Melling A, Whitelaw JH (1974) Low Reynolds number flow over a plane symmetric sudden expansion. J Fluid Mech 64:111–128

Ehlert S, Hlushkou D, Tallarek U (2008) Electrohydrodynamics around single ion-permselective glass beads fixed in a microfluidic device. Microfluid Nanofluid 4:471–487

Ferzieger JL, Peric M (1996) Computational methods for fluid dynamics. Springer-Verlag, Heidelberg

Gerlach T, Schuenemann M, Wurmus H (1995) A new micropump principle of the reciprocating type using pyramidic micro flowchannels as passive valves. J Micromech Microeng 5:199–201

Hsu CJ, Sheen HJ (2008) A microfluidic flow-converter based on a double-chamber planar micropump. Microfluid Nanofluid. doi: 10.1007/s10404-008-0347-8

Hsu Y, Lin S, Hou S (2007) Development of peristaltic antithrombogenic micropumps for in vitro and ex vivo blood transportation tests. Microsyst Technol 14:31–41

Hwang IH, Lee SK, Shin SM, Lee YG, Lee JH (2008) Flow characterization of valveless micropump using driving equivalent moment: theory and experiments. Microfluid Nanofluid 5:795–807

Issa RI (1986) Solution of implicitly discretized fluid flow equations by operator splitting. J Comput Phys 62:40–65

Iverson BD, Garimella SV (2008) Recent advances in microscale pumping technologies: a review and evaluation. Microfluid Nanofluid 5:145–174

Jang L, Kan W (2007) Peristaltic piezoelectric micropump system for biomedical applications. Biomed Microdev 9:619–626

Kawahashi M, Tamotsu F, Saito M (2007) Acoustic Fluid Machine, US Pat. No. 7252178 B2

Kurzweg UH, Lindgren ER, Lothrop B (1989) Onset of turbulence in oscillating flow at low Womersley number. Phys Fluids A 12:1972–1975

Morris CJ, Forster FK (2004) Oscillatory flow in microchannels: comparison of exact and approximate impedance models with experiments. Exp Fluids 36:928–937

Nguyen B, Kassegne SK (2008) High-current density DC magenetohydrodynamics micropump with bubble isolation and release system. Microfluid Nanofluid 5:383–393

Olsson A, Stemme G, Stemme E (1999) A numerical design study of the valveless diffuser pump using lumped-mass mode. J Micromech Microeng 9:34–44

Park HM, Lim JY (2008) A reduced-order model of the low-voltage cascade electroosmotic micropump. Microfluid Nanofluid. doi: 10.1007/s10404-008-0326-0

Patankar SV (1980) Numerical heat transfer and fluid flow. Hemisphere, Washington, DC

Pan LS, Ng TY, Liu GR, Lam KY, Jiang TY (2001) Analytical solution for the dynamic analysis of a valveless micropump: afluid-membrane coupling study. Sens Actuators A Phys 93:173–181

Sheen HJ, Hsu CJ, Wu TH, Chang CC, Chu HC, Yang CY, Lei U (2008) Unsteady flow behaviors in an obstacle-type valveless micropump by micro-PIV. Microfluid Nanofluid 4:331–342

Singhal V, Garimella SV, Murthy JY (2004) Low Reynolds number flow through nozzle/diffuser elements in valveless micropumps. Sens Actuators A Phys 113:226–235

Sun CL, Huang KH (2006) Numerical characterization of the flow rectification of dynamic microdiffusers. J Micromech Microeng 16:1331–1339

Sun CL, Yang ZH (2007) Effects of the half angle on the flow rectification of a microdiffuser. J Micromech Microeng 17:2031–2038

Stemme E, Stemme G (1993) A valveless diffuser/nozzle-based fluid pump. Sens Actuators A Phys 39:159–167

Tsui YY, Lu SL (2008) Evaluation of the performance of a valveless micropump by CFD and lumped-system analyses. Sens Actuators A Phys 148:138–148

Tsui YY, Wang HW (1995) Calculation of laminar separated flow in symmetric two-dimensional diffusers. J Fluid Eng 117:612–616

Wang YC, Hsu JC, Kuo PC, Lee YC (2009) Loss characteristics and flow rectification property of diffuser valves for micropump applications. Int J Heat Mass Transfer 52:328–336

Wu J, Ben Y, Chang HC (2005) Particle detection by electrical impedance spectroscopy with asymmetric-polarization AC electroosmotic trapping. Microfluid Nanofluid 1:161–167

Yang KS, Chen IY, Shew BY, Wang CC (2004) Investigation of the flow characteristics within a micronozzle/diffuser. J Micromech Microeng 14:26–31

Zhang C, Xing D, Li Y (2007) Micropumps, microvalves, and micromixers within PCR microfluidic chips: advances and trends. Biotechnol Adv 25:483–514